




Article

Solution Processed NiO/MoS₂ Heterostructure Nanocomposite for Supercapacitor Electrode Application

Dhivyaprasath Kasinathan ¹, Praveena Prabhakar ¹, Preethi Muruganandam ¹, Biny R. Wiston ¹,
Ashok Mahalingam ^{1,*} and Ganesan Sriram ^{2,*}

¹ New Generation Materials Laboratory, Department of Physics, National Institute of Technology, Tiruchirappalli 620015, India

² School of Chemical Engineering, Yeungnam University, Gyeongsan 38541, Republic of Korea

* Correspondence: ashokm@nitt.edu (A.M.); sriramyu@yu.ac.kr (G.S.)

Abstract: Metal oxide and metal dichalcogenide heterostructure composites are promising candidates for electrochemical use. In this study, a hybrid heterostructure composite electrode material was made using a straightforward hydrothermal process using transition metal oxide (NiO) and metal dichalcogenide (MoS₂). The surface of the flower-like structured MoS₂ was grown with granular structured NiO, and this heterostructure composite exhibited considerably improved specific capacitance when compared to the pure NiO and MoS₂ materials. The pseudocapacitive performance was effectively supported by the heterostructure combination of transition metal oxide (TMOs) and metal dichalcogenide (MDC), which greatly improved ion transport within the material and storage. At a current density of 1 A/g, the prepared heterostructure composite electrode material exhibited a specific capacitance of 289 F/g, and, after 2000 cycles, the capacitance retained 101% of its initial value. The symmetric device was constructed and put through tests using LED light. This finding opens up a new avenue for the quickly increasing the field of heterostructure materials.

Keywords: heterostructure composite; NiO supercapacitor; TMO–TMC composite; MoS₂ supercapacitor



Citation: Kasinathan, D.; Prabhakar, P.; Muruganandam, P.; Wiston, B.R.; Mahalingam, A.; Sriram, G. Solution Processed NiO/MoS₂ Heterostructure Nanocomposite for Supercapacitor Electrode Application. *Energies* **2023**, *16*, 335. <https://doi.org/10.3390/en16010335>

Academic Editor: Kwang-Sun Ryu

Received: 21 November 2022

Revised: 23 December 2022

Accepted: 24 December 2022

Published: 28 December 2022



Copyright: © 2022 by the authors. Licensee MDPI, Basel, Switzerland. This article is an open access article distributed under the terms and conditions of the Creative Commons Attribution (CC BY) license (<https://creativecommons.org/licenses/by/4.0/>).

1. Introduction

The world's energy demands have rapidly expanded over time, yet the majority of that energy still comes from fossil fuels [1]. Dependence on fossil fuels for an extended period of time is not recommended since it increases the greenhouse effect, which causes ozone depletion and global warming [2]. Renewable energy generation and powerful storage technologies are essential for replacing fossil fuel energy. Solar cells, hydropower, and windmills are just a few examples of the renewable energy sources that may be harnessed for use in the energy industry. A gadget that can store energy generated from renewable sources for later use is required. Fuel cells, batteries, capacitors, and so on are only some of the various energy storage options available. Nevertheless, the combination of high energy density and high power density in supercapacitors or ultracapacitors makes this area of study intriguing. In addition, there are three distinct types of supercapacitors that differ based on the process by which they store a charge: pseudocapacitors, electrochemical double-layer capacitors (EDLC), and hybrid capacitors [3]. Depending on the sort of energy storage mode used by the supercapacitor, the electrode material varies [4]. For instance, carbon-type materials such as carbon nanotubes, carbon aerogels, etc. are used in EDLC, but metal-based compounds such as metal oxide, metal chalcogenides, metal nitrides, etc. are used in pseudocapacitors [5–7]. A hybrid capacitor utilizes both an EDLC and a pseudocapacitor.

The transition metal oxides MnO₂, V₂O₅, NiO, Co₃O₄, Fe₃O₄, and SnO₂ exhibit capacitance characteristics [8–14]. Among these metal oxides, NiO is the most attractive choice because of its low to high capacitance, stability, low cost, and strong electrochemical activity. Recently, Vijayakumar et al. used the microwave method to produce NiO

nanoflakes and reached 409 F/g at 0.5 current density [15]. In another investigation, Dhas et al. produced NiO using a simple hydrothermal technique and achieved 132 F/g at a scan rate of 5 mV/s [16]. Pore et al. recently created a hydrothermally generated NiO/rGO nanocomposite and achieved 727.1 F/g at 1 mA/cm² current density [17]. However, owing to weak electrical conductivity and a small accessible surface area, it has not been possible to achieve the predicted specific capacitance value of 2584 F/g [18]. To address the aforementioned problem, van der Waals heterostructures, composites of various nanostructured materials with exceptional qualities, were developed by combining metal chalcogenides with metal oxides [19,20]. In compounds known as transition metal dichalcogenides, the metal acts as a cation, while chalcogens such as sulfur, selenides, and other similar elements serve as anions. Metal oxides, on the other hand, are composed of a metal cation and an oxygen anion. Molybdenum disulfate (MoS₂) is one of the transition metal dichalcogenides (TMD), and it has a particularly desirable performance in the area of electrochemical energy storage and conversion. MoS₂ has a unique 2D structure that provides ions with a lot of surface accessibility; the different oxidation states of the Mo atoms enable those accessible ions to store energy. Additionally, for charge storage, the layered structure of MoS₂ (S-Mo-S) with van der Waals forces gives sufficient space to allow in the external ions between the layers [21].

Recent research conducted by Acerce and colleagues explored chemically exfoliated metallic 1T phase MoS₂ nanosheets. The researchers conducted electrochemical studies using various ions, such as H⁺, Li⁺, Na⁺, and K⁺, and they achieved capacitance ranging from 400 to 700 F/cm³. In addition, the material stability was maintained at 95% after 5000 cycles [22]. Joseph et al., using the hydrothermal process, synthesized metallic defect induced active edge 1T-MoS₂ and investigated its electrochemical activity. They attained 379 F/g at a current density of 1 A/g, and the material maintained 92% of its stability after 3000 cycles [23]. In their hydrothermal synthesis of metallic MoS₂, Geng et al. observed a specific capacitance of 380 F/g when scanned at a rate of 5 mV/s [24]. Ghasemi et al. developed a NiO/MoS₂/rGO composite and employed it as a supercapacitor electrode; after 1000 cycles, the capacitance was 7.38 mF/cm² with 90% retention [25]. Li et al. developed a Ni(OH)₂/MoS₂ nanohybrid with a specific capacitance of 201 mAh/g at a scan rate of 5 mV/s and capacitance retention of 83% at a current density of 20 A/g [26]. Luo et al. developed a Ni₃S₄-MoS₂ heterojunction electrode using a simple hydrothermal process; electrochemical measurements revealed a specific capacitance of 985.25 F/g at a current density of 1 A/g, as well as a capacitance retention of 58% after 20,000 cycles at a current density of 10 A/g [27]. Yue et al. developed a Ni metal organic framework (MOF) and a composite with MoS₂; an electrochemical analysis revealed a remarkable specific capacitance of 1590.24 F/g at a current density of 1 A/g, with capacitance preserved at 88% after 20,000 cycles at a current density of 5 A/g [28]. In the field of supercapacitors, NiO and MoS₂ are both adaptable; in addition, their lateral resemblance increases the potential of heterostructure composites, which have improved electric pseudocapacitive and electric double-layer capacitive performances, simultaneously. The benefit of a heterostructure is improved electrical performance in comparison to pristine materials; various metal oxides have numerous redox activities. In addition, hybridization results in an increased surface area and decreased diffusion length [29,30]. As a result, the NiO-MoS₂ heterostructure composition could be used as an electrode material for supercapacitors. It also has more structural deficiencies and a greater number of accessible electrochemical active sites for ion/electron diffusion, which enhances the redox reaction activities and electrochemical energy storage [19,30,31].

In this study, it was shown that the hydrothermal process was used to create MoS₂ with a flower-like structure. A thin layer of NiO was then formed on the prepared MoS₂ surface after it was dissolved in water. The hybrid behavior of an electrochemical supercapacitor and an EDLC was investigated using this NiO-MoS₂ heterostructure composite. Throughout the whole electrochemical study, an economical graphite sheet was used and showed good capacitance.

2. Materials and Methods

2.1. Synthesis of MoS₂

MoS₂ was produced using the hydrothermal technique, which included dissolving 0.02 M of ammonium molybdate in 70 mL of double-distilled (DD) water first and then gradually adding 0.08 M of thiourea to the solution while stirring continuously at room temperature. The mixture was stirred for an additional 30 min. Then, the solution was transferred to a 100 mL stainless steel Teflon inline autoclave and held there for 24 h at 180 °C. Additionally, the precipitate was collected, washed with DD water and ethanol, and then dried overnight at 60 °C. The collected sample was labeled as M.

2.2. Synthesis of NiO and NiO-MoS₂ Composite

As with a typical procedure, 180 mg of MoS₂ was dispersed in 60 mL of DD water. Following that, 0.1 M of nickel nitrate hexahydrate (Ni (NO₃)₂·6H₂O) was added and dissolved. The pH of the solution was then adjusted to 11 using the NH₃OH solution. The solution was then transferred to a 100 mL Teflon inline autoclave and put in a furnace, where it was heated at 150 °C for 12 h. The precipitate was recovered and washed multiple times with DD water followed by ethanol before being dried in a vacuum oven at 60 °C for 6 h. Next, the dried powder was annealed at 450 °C for 1 h. Then, the collected sample was labeled as NM3. The same procedure was followed with 600 mg of MoS₂, and the sample was labeled as NM10; without MoS₂, pure NiO was prepared and labeled as N.

2.3. Working Electrode Preparation and Electrochemical Studies

To make the working electrodes, active material (N, M, NM3, and NM10) was ground with acetylene black (AB) and polyvinylidene difluoride (PVDF) in a ratio of 80:10:10 with 1-methyl-2-pyrrolidinone (NMP). The produced slurry was coated on a graphite sheet in an area that measured about 1 × 1 cm² and was then dried at 90 °C for 6 h. Three electrodes and 1M KOH were employed as the electrolyte to investigate the active material's electrochemical behavior. The prepared material's electrochemical activity was analyzed using the following methods: cycle stability, electrochemical impedance spectroscopy (EIS), galvanostatic charge discharge (GCD), and cyclic voltammetry (CV). With a three-electrode potentiostat Palmsens 3 (PSTrace 5.9, EKTechnologies GmbH, Nufingen, Germany) equipment in an ambient environment, a full electrochemical investigation was carried out. The constructed electrode was used as the working electrode, Ag/AgCl in 3.5 M KCl served as the reference electrode, and a platinum wire served as the counter electrode in the electrochemical investigation.

2.4. Instrumentation

The crystal structure of the materials was studied by X-ray diffraction using an Ultima III with Cu-Kα wavelength of $\lambda = 1.54056 \text{ \AA}$ at potential of 40 kV. The vibrational studies were performed with Fourier transform infrared spectroscopy (FTIR) by a Thermo scientific Nicolet iS5, Massachusetts, United States in KBr mode in the range of 400 to 4000 cm⁻¹ wavenumbers. The morphology of materials was analyzed by field emission scanning electron microscopy (FESEM) with energy dispersive X-ray spectroscopy (EDX) obtained with a GEMINI 300, Carl Zeiss, Oberkochen Germany; the sample was dispersed on the top of a carbon-coated grid. Transmission electron microscopy (TEM) was obtained with a Tecnai G230S. The thermal stability of the materials was analyzed by thermogravimetric analysis (TGA) performed by an Exstar 6200 TG/DTA instrument, LabWrench, Midland, ON, Canada.

3. Results and Discussion

3.1. Structural Characterizations

X-ray diffraction was used to examine the structural analyses of the produced pristine N and M and nanocomposite NM3 and NM10, which are shown in Figure 1a. In the NiO spectrum, major peaks were observed at $2\theta = 37.52^\circ, 43.54^\circ, 63.12^\circ, 75.70^\circ, \text{ and } 79.56^\circ$

belonging to the planes (111), (200), (220), (311), and (222) for an NiO cubic structure with a JCPDS card no. 47-1049 [32]. For the MoS₂ spectrum, major peaks were observed at $2\theta = 14.36^\circ, 33.58^\circ, 40.02^\circ, 44.04^\circ, 49.76^\circ,$ and 59.04° , which corresponded to planes (002), (100), (103), (006), (105), and (008) with JCPDS card no. 37-1492 [33–35].

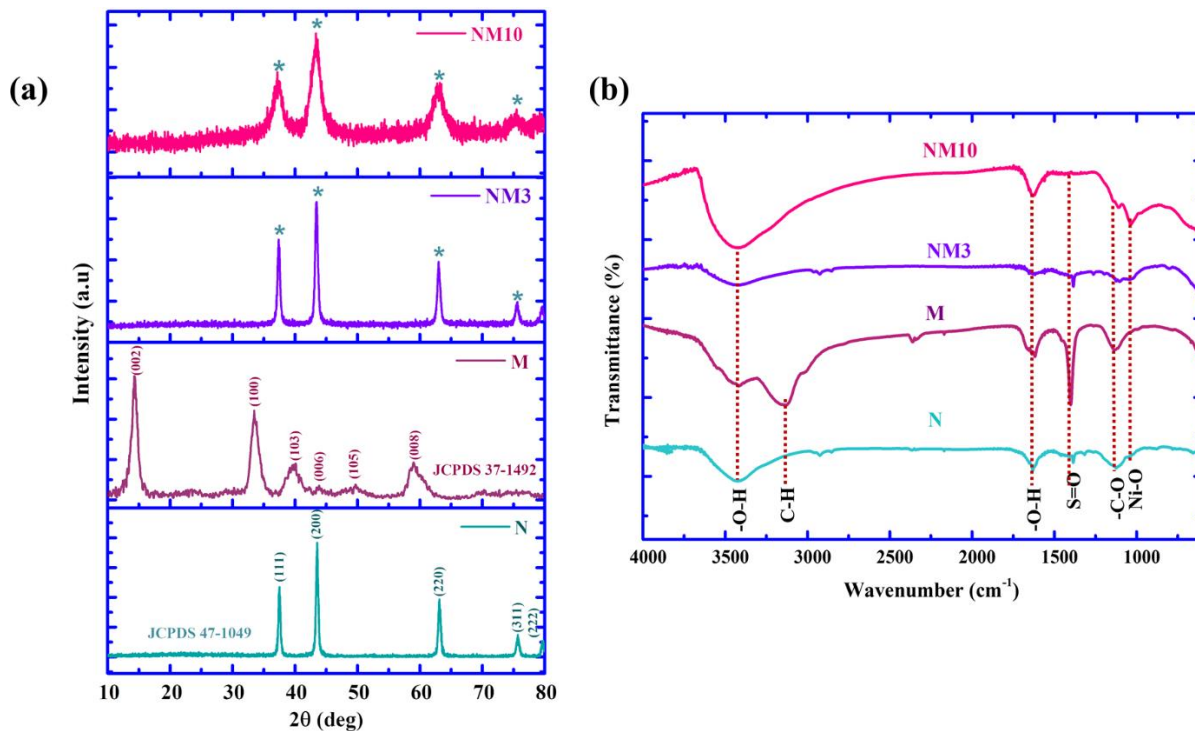


Figure 1. (a) X-ray diffraction pattern of N, M, NM3, and NM10; (b) FTIR spectra of N, M, NM3, and NM10; * is the NiO peak in composite.

The NM3 spectrum and pure NiO showed no significant changes. Because MoS₂ has a lower diffraction density than the other materials, the NM10 composite did not detect the MoS₂ peak. Additionally, the crystallinity of the composite was lower than that of the pristine material, and it was noted that the material's full width at half maxima had risen [36,37].

From the following Scherrer's formula, the crystallite size of the materials was calculated [38].

$$D = \frac{K\lambda}{\beta \cos \theta} \quad (1)$$

where D is the crystallite size, K is the crystallite shape factor, λ is the wavelength of the X-ray, β is the full width at half maxima, and θ is the Bragg's angle. The crystallite size of pure NiO is 20.56 nm; but, after being combined with MoS₂, it only measured 2.90 nm. This is because MoS₂ has a lower crystallinity than NiO.

The molecular vibrations of samples N, M, NM3, and NM10 were analyzed from FTIR spectra, as shown in Figure 1b. In the sample N spectrum, the typical peak at 1125 cm^{-1} indicated a C-O stretching vibration. The peak at 1630 and 3440 cm^{-1} corresponded to the O-H bending vibration. The peak at 1397 cm^{-1} represented an S=O stretching vibration. The minor peak at 3144 cm^{-1} corresponded to the asymmetric vibration of C-H stretching. The peak at 1039 cm^{-1} represented Ni-O bending [39–42]. The FTIR spectra of M, NM3, and NM10 had similar vibrations as C-O stretching, H₂O deformation, OH bending, and C-H stretching at identical scales. In summary, diffraction peaks of MoS₂ were not reflected in the composite, while the crystallinity of the material was lowered for the composite. This is because the crystallinity density of MoS₂ is smaller than that of NiO. In the FTIR, the presence of MoS₂ was confirmed with the S=O stretching vibration and C-O stretching.

3.2. Morphological Studies

SEM investigation revealed the surface morphology of synthesized N, M, NM3, and NM10, as shown in Figure 2a–d. Sample N was found to have tiny sphere-like particles (Figure 2a). On the other hand, M had a cluster of nanoflower structures. NiO can be seen forming on the surface of the MoS₂ nanoflower in NM3 and NM10 (Figure 2c,d). In order to improve charge mobility and increase electrochemical activity, the surface flower-like structure of the MoS₂ particles was grown on by the nanoscale sphere-shaped NiO.

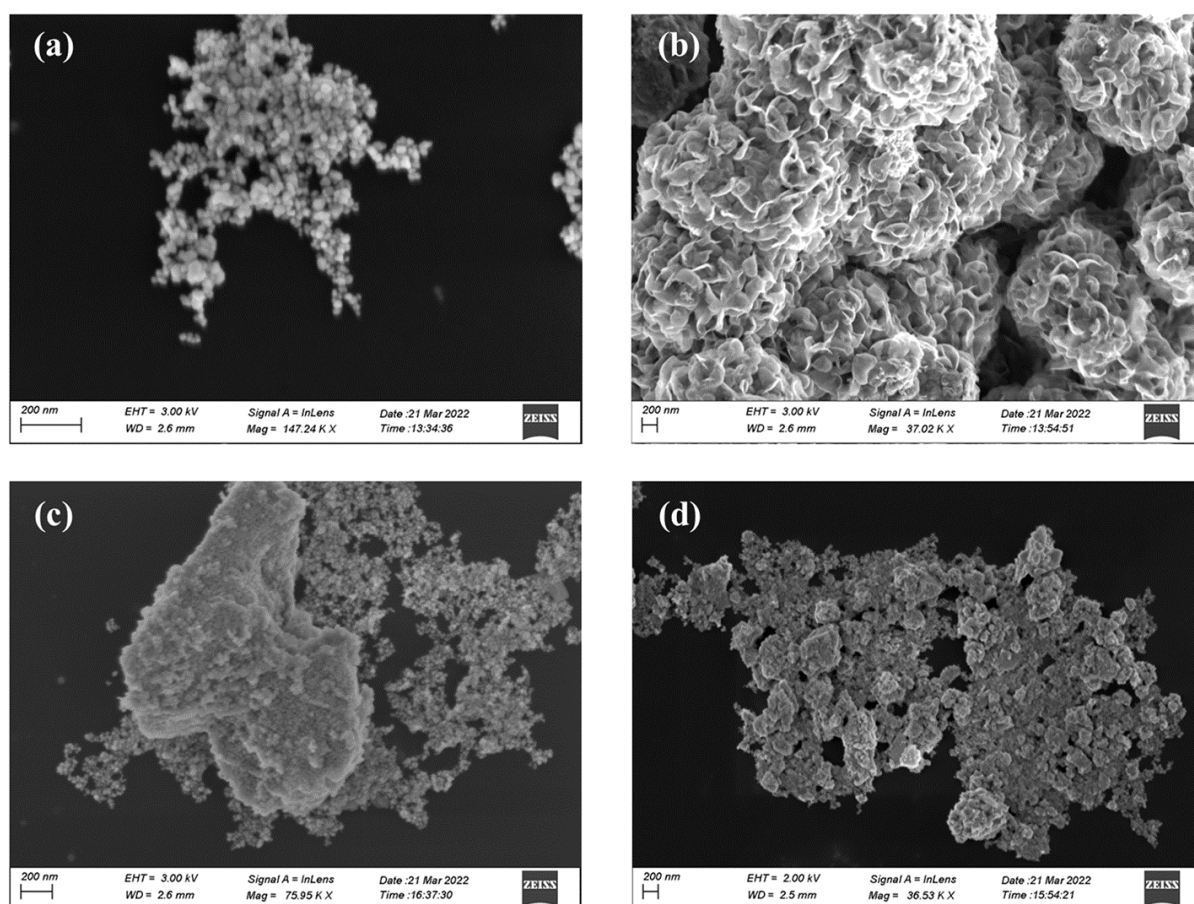


Figure 2. FESEM images of (a) N, (b) M, (c) NM3, and (d) NM10.

The corresponding TEM pictures showed the pure NiO and NiO-MoS₂ composite nanostructures (Figure 3a–e); their electron diffraction images are shown in Figure 3c,f, respectively. According to the observed TEM images, N had particles that were about 22 nm in size, some of which were clustered when viewed from a distance, and others had a hexagonal shape to them. Similarly, NM10 particles had a size of 1.2 μm and they had two distinct parts: one was the MoS₂ nanoflower's core and the other was the NiO that formed on the nanoflower's surface. The SAED pattern of the N and NM10 demonstrated a decrease in crystallinity from N to NM10 and was in agreement with the XRD findings.

3.3. Elemental Analysis

The prepared N, M, NM3, and NM10 elemental analyses are shown in Figure 4a–d. Sample N verified the presence of nickel and oxygen with weight percentages of 75.8% and 25.2%, respectively. Sample M verified the presence of molybdenum and sulphur with percentages of 55.2% and 44.8%, respectively. The elemental mapping of the sample NM3 revealed the presence of a large quantity of nickel and oxygen and a very little amount of molybdenum and sulphur, with weight percentages of 57%, 41%, 1%, and 1%, respectively. It validated the little quantity of MoS₂ contained in the composite. Nickel, oxygen, molyb-

denum, and sulphur were likewise contained in NM10 in the proportions of 73%, 24%, 2%, and 1%, respectively. The EDX energy spectrum is displayed in Figure S1 and the composition is listed in Table S3. These decreased Mo and S weight percentage concentrations demonstrated that the NiO was formed on the surface of the MoS₂ nanoflowers.

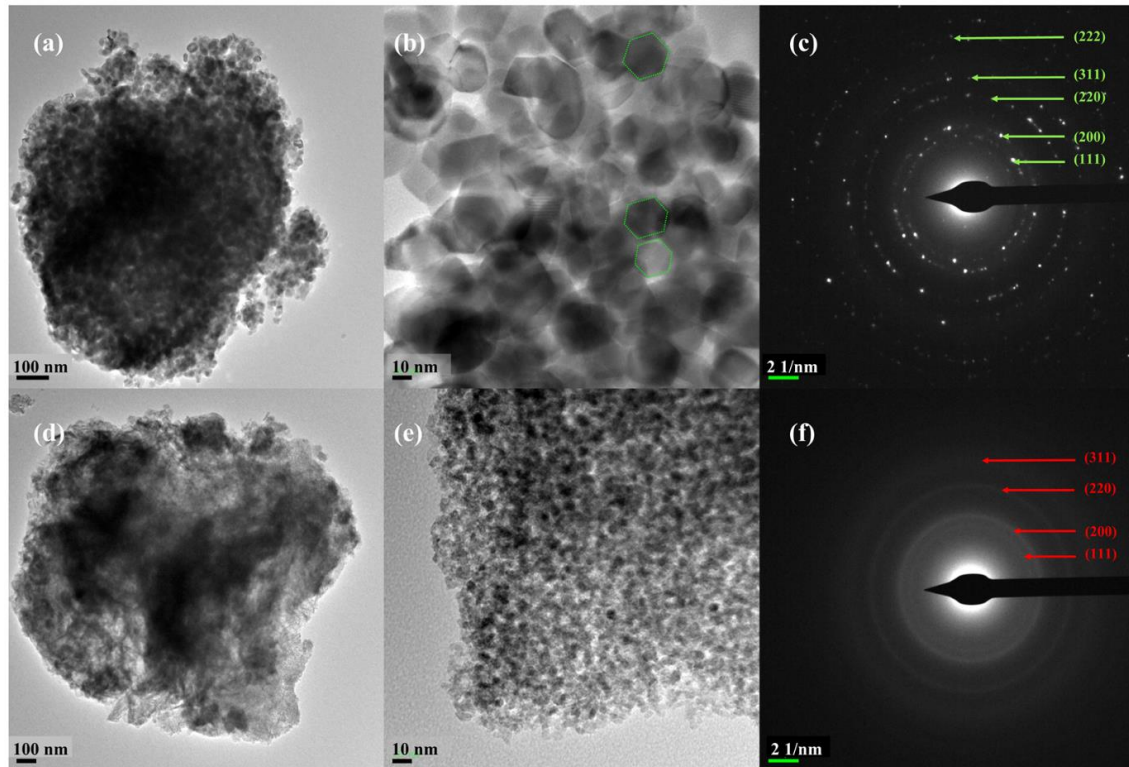


Figure 3. TEM images of N (a,b), NM10 (d,e), and electron diffraction pattern of N (c) and NM10 (f).

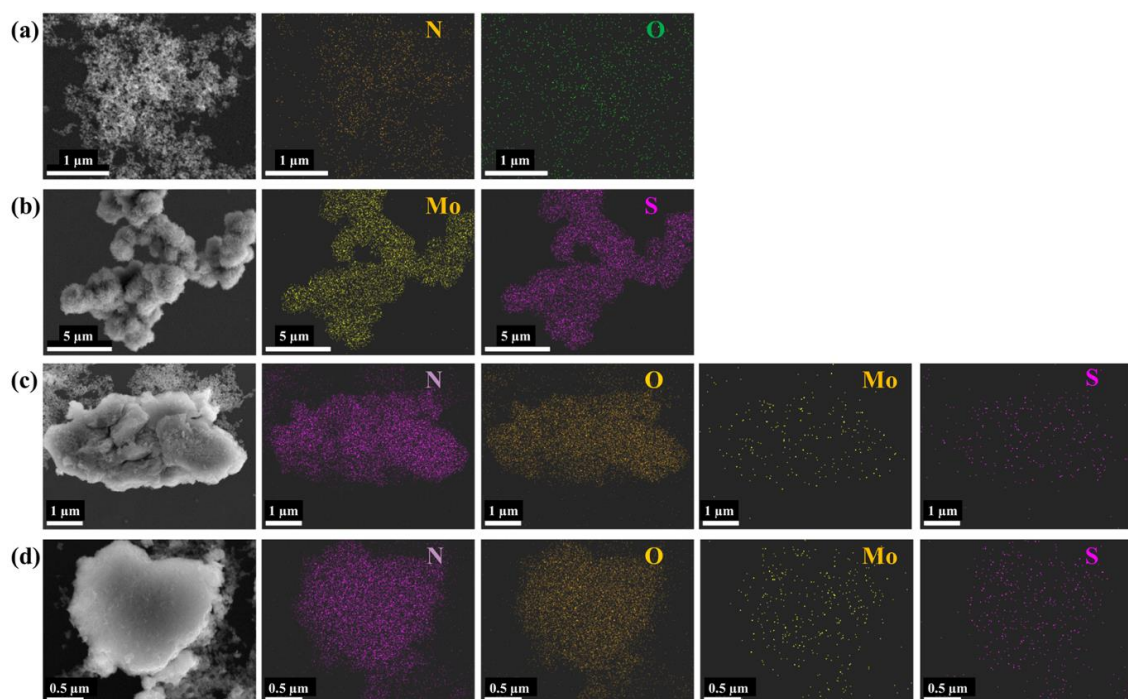


Figure 4. EDX elemental mapping of (a) N, (b) M, (c) NM3, and (d) NM10 composite nanoparticles.

3.4. Electrochemical Characterizations

Electrochemical methods such as cyclic voltammetry (CV), galvanostatic charge and discharge (GCD), electrochemical impedance spectroscopy (EIS), and stability testing were used to investigate the electrochemical activity of synthesized materials. In an aqueous electrolyte 1 M KOH solution, the CV of N, M, NM3, and NM10 was measured in a three-electrode setup with a potential window of 0–0.65 V vs. Ag/AgCl. Figure 5 depicts CV curve at various scan rates of 5, 10, 15, 20, 25, 30, 35, and 40 mVs^{-1} .

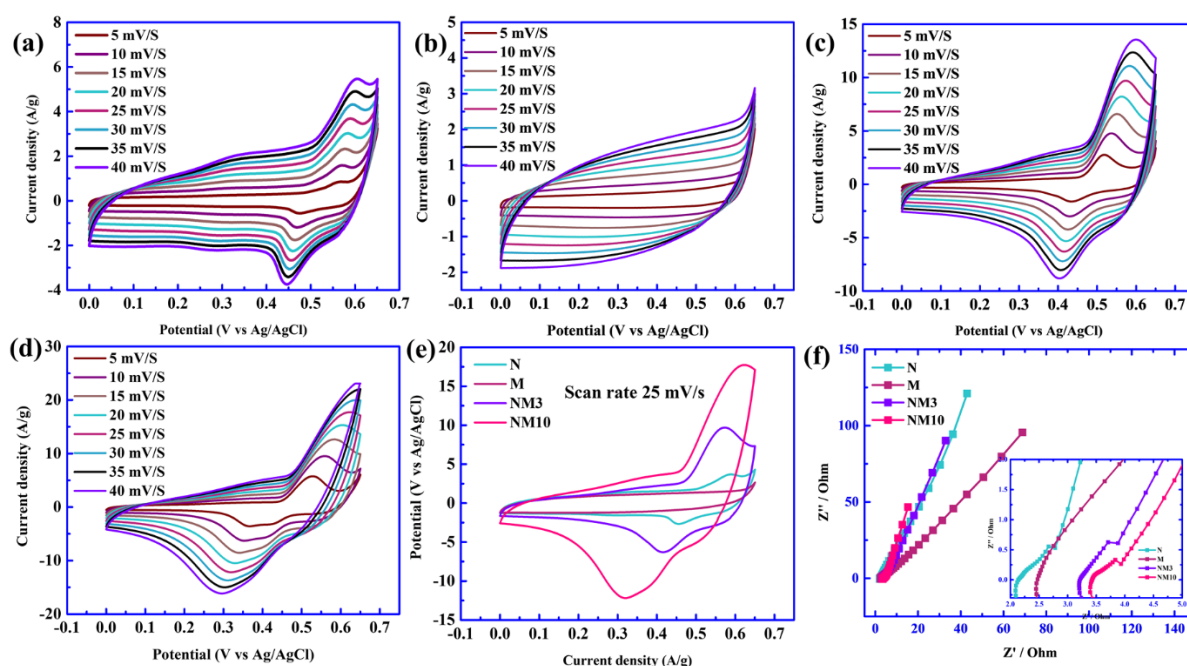
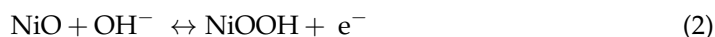


Figure 5. (a–d) CV curves of N, M, NM3, and NM10 with different scan rates; (e) comparison of CV curves of N, M, NM3, and NM10 with a scan rate of 25 mV/s ; (f) EIS spectra of N, M, NM3, and NM10 (inside image is an enlarged high-frequency region).

The current peaks were found during cathodic and anodic scans, and their current density rose with the scan rate without altering the form at higher scan rates. They depicted the electrons' and ions' fast moments during the redox reaction, and they determined the quick insertion and exertion of the ions at the electrode surface [43]. According to the CV curves, pristine NiO and MoS_2 exhibited a faradic redox reaction behavior and electrochemical double-layer capacitor (EDLC) combined with pseudocapacitive behavior, respectively, whereas the composite exhibited a dominating faradic redox reaction behavior [44,45]. The following redox reaction was possible between the working electrode and alkaline aqueous solution [31,46].



The specific capacitance (C_{sp}) of electrode materials from the CV curve was calculated by following the formula [47]:

$$C_{\text{sp}} = \frac{1}{mv(V_b - V_a)} \int_{V_a}^{V_b} I dV \quad (3)$$

where C_{sp} is the specific capacitance (Figure 1), v is the scan rate (mVs^{-1}), m is the mass of the active material (g), V_b and V_a are the CV potential window limits (V), and I is the discharge current (A). The material's specific capacitance was estimated from the CV curve and is listed in Table S1.

The GCD studies were explored by varying the current density from 0.25 Ag^{-1} to 2 Ag^{-1} with a potential of 0.57 V . The results of these investigations are shown in Figure 6a–d. The GCD profile of pure NiO suggests that the material behaved as a pseudocapacitor, whereas the EDLC profile of MoS_2 was dependent on the composite. Pseudocapacitance was dominated by NM3 and NM10, however. Figure 6e presents a comparison of the GCD curve with 0.5 Ag^{-1} . Based on the GCD curve, the specific capacitance of the electrode may be calculated using the following formula [48]:

$$C_{\text{sp}} = \frac{I dt}{m dV} \quad (4)$$

where I is the discharge current (A), dt is the discharge time (s), m is the mass of active material (g), dV is the potential window (V), and C_{sp} is the specific capacitance (Fg^{-1}). N, M, NM3, and NM10 were found to have specific capacitances of 86, 56, 126, and 289 Fg^{-1} , respectively, at 1 Ag^{-1} current density. The capacitance retention of N, M, NM3, and NM10 was observed at 95.7%, 90.4%, 98.6%, and 101.6%, respectively, during the GCD cyclic stability test at 1 A/g for 2000 cycles. According to the aforementioned findings, pristine material exhibited lower capacitance and stability, while composite materials exhibited higher capacitance and stability. This is because heterostructure materials provide advantages including high ion migration, large surfaces, and more active sites. These characteristics provide easier charging and draining conditions and more charge storage. Table S2 contains the material's specific capacitance as determined from the GCD curve. The specific capacitance significantly reduced at higher scan rates because of increased ion diffusion on the electrode's inner structure and a lowered interface between the electrolyte and active material. As a result, electrolyte ions quickly reached the current collector. Higher current density reduced the amount of electrode surface that the ions could reach, which lowered the specific capacitance. Comparisons of the specific capacitances at various current densities are shown in Figure S2.

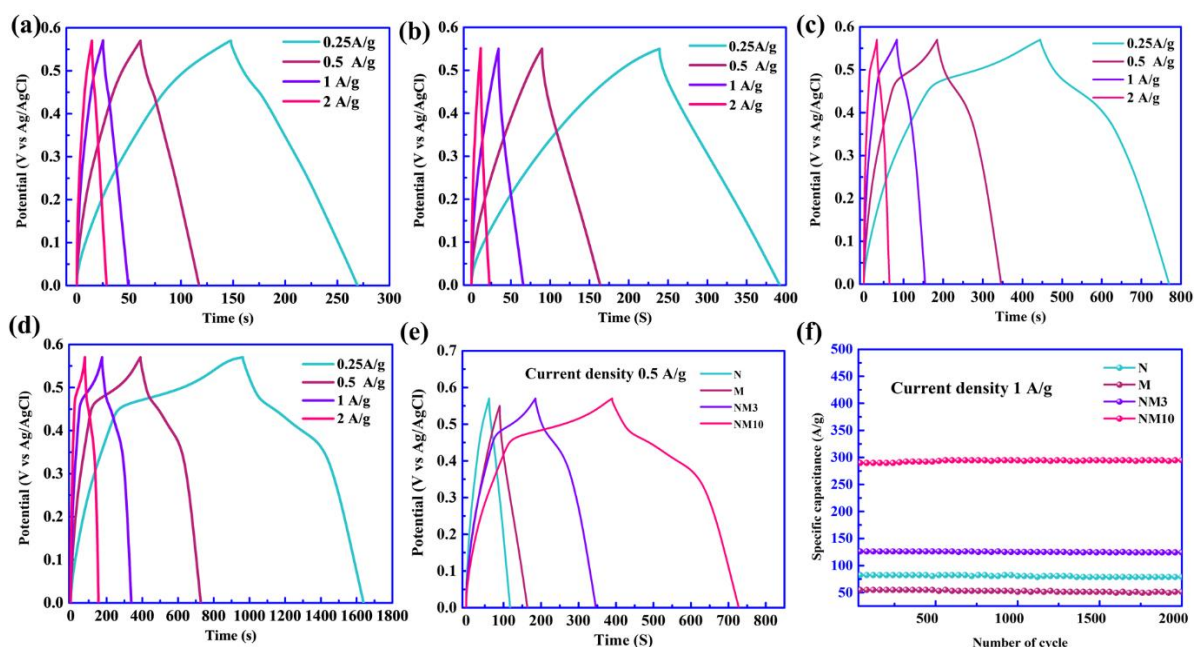


Figure 6. (a–d) GCD curves of N, M, NM3, and NM10, respectively, with various current densities; (e) comparison of GCD for N, M, NM3, and NM10 with 0.5 current density; (f) GCD stability of N, M, NM3, and NM10 at 1 A/g current density for 2000 cycles.

The coated electrode's EIS was carried out at 0.5 V at frequencies of 10 kHz to 0.1 Hz ; their Nyquist curves are shown in Figure 5f. These graphs demonstrate the electrode's resistance characteristics. The electrode exhibited a small curve in the high-frequency region

of the Nyquist plot, indicating that the faradaic reaction occurred at the electrode–electrolyte interface. At low frequencies, however, the straight line was seen because of Warburg impedance. The plot's 45° angle clearly showed how the electrode behaved capacitively. In comparison to N, M, and NM3, the NM10 electrode had the lowest resistance, indicating that it has better conductivity and is more appropriate for use in supercapacitors. The best electrode's material stability was assessed for 2000 cycles using a current density of 1 Ag^{-1} , as shown in Figure 6f. After 2000 consecutive GCD cycles, it was seen that the specific capacitance rose; the electrode now had 101.5% more capacitance than before. This might be because the electrolyte ions were more easily able to reach the active sites on the electrode surface.

NiO was grown on the surface of the flower-like MoS_2 possible mechanism of schematic illustration and electrode–electrolyte interface, as shown in Figure 7. The unique flower-like structure of the NiO– MoS_2 composite may increase the active site and allow for easier storage of the hydroxyl ion (OH^-) on the surface of the electrode. In addition, the improved charge conductivity may increase quick transport on the electrode surface. In Table 1, the specific capacitance cyclic stability was compared to earlier studies. According to the results above, the composite of NiO– MoS_2 exhibited more electrochemical activity than the pristine materials.

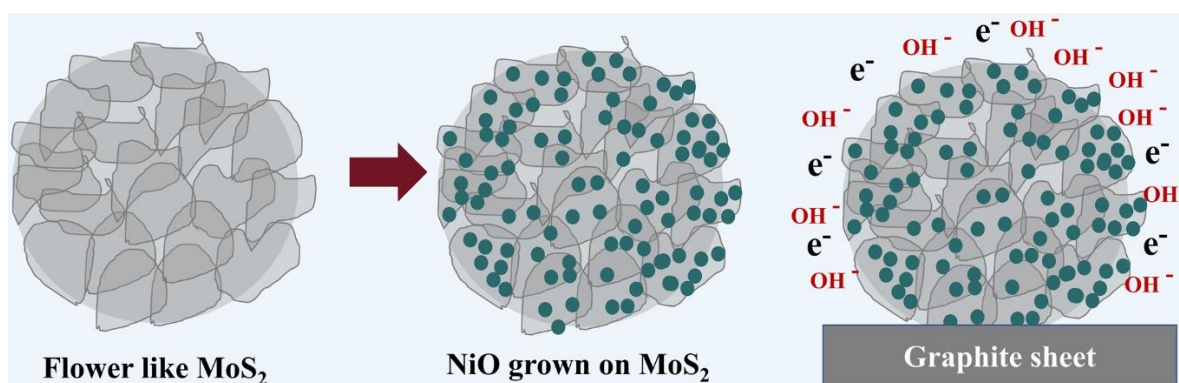


Figure 7. Growth mechanism and charge storage reaction at the electrode and electrolyte surface.

Table 1. Specific capacitance comparing similar work and carbon-based electrode materials.

Material	Current Density or Scan Rate	Electrolyte	Specific Capacitance	Retention	Reference
NiO nanoflakes	0.5 Ag^{-1}	2 M KOH	409 Fg^{-1}	92% after 500 cycles at current density 10 Ag^{-1}	[15]
NiO nanoparticles	5 mVs^{-1}	1 M KOH	132 Fg^{-1}	75% after 500 cycles at scan rate 5 mVs^{-1}	[16]
NiO/rGO composite	1 mAcm^{-2}	6 M KOH	727.1 Fg^{-1}	80% after 9000 cycles at current density 1 mAcm^{-2}	[17]
Metallic 1T- MoS_2	1 Ag^{-1}	1 M KOH	379 Fg^{-1}	92% after 3000 cycles at current density 1 A/g	[23]
$\text{Ni(OH)}_2/\text{MoS}_2$	5 mVs^{-1}	6 M KOH	201 mAhg^{-1}	83% after 3000 cycles at current density 20 A/g	[26]
$\text{Ni}_3\text{S}_4\text{-MoS}_2$	1 Ag^{-1}	3 M KOH	982.21 Fg^{-1}	58% after 20,000 cycles at current density 10 Ag^{-1}	[27]
Ni-MOF @ MoS_2	1 Ag^{-1}	3 M KOH	1590.24 Fg^{-1}	88% after 20,000 cycles at current density 5 Ag^{-1}	[28]
NiO nanobelts	5 Ag^{-1}	2 M KOH	660 Fg^{-1}	95% after 2000 cycles at current density 5 Ag^{-1}	[46]

Table 1. Cont.

Material	Current Density or Scan Rate	Electrolyte	Specific Capacitance	Retention	Reference
Ni ₉ S ₈ /O-MoS ₂ nanocomposite	2 Ag ⁻¹	1 M KOH	907 Fg ⁻¹	86% after 1200 cycles at current density 2 Ag ⁻¹	[49]
MoS ₂ /NiS	2 Ag ⁻¹	6 M KOH	1165 Fg ⁻¹	100% after 10,000 cycles at current density 0.5 Ag ⁻¹	[50]
Chitin-derived activated carbon	0.5 Ag ⁻¹	1 M H ₂ SO ₄	227 Fg ⁻¹	98% after 10,000 cycles at current density 10 Ag ⁻¹	[51]
MnO@CNP-2 hybrid electrode	0.5 Ag ⁻¹	6 M KOH	545 Fg ⁻¹	87% after 3000 cycles at current density 10 Ag ⁻¹	[52]
Chitosan porous carbon spheres/MXene	0.5 Ag ⁻¹	1 M H ₂ SO ₄	362 Fg ⁻¹	98% after 10,000 cycles at current density 10 Ag ⁻¹	[53]
Hierarchical porous polyimide-derived carbon (CPC-Fe/Zn)	1 Ag ⁻¹	6 M KOH	420 Fg ⁻¹	92% after 1000 cycles at current density 20 Ag ⁻¹	[54]
Camellia pollen activated carbon	1 Ag ⁻¹	6 M KOH	280 Fg ⁻¹	85% after 20,000 cycles at current density 20 Ag ⁻¹	[55]
Porous carbon N-doped	0.5 Ag ⁻¹	6 M KOH	275 Fg ⁻¹	95% after 5000 cycles at current density 5 Ag ⁻¹	[56]
NiO-MoS ₂ heterostructure	1 Ag ⁻¹	1 M KOH	289 Fg ⁻¹	101% after 2000 cycles at current density 1 Ag ⁻¹	This work

4. Conclusions

In conclusion, a straightforward hydrothermal approach proved effective in producing the heterostructure NiO-MoS₂ composite. In comparison to the pristine material, the produced composite exhibited decreased crystallinity and a governed NiO cubic structure with an average crystallite size of 2.90 nm. The composite was confirmed by vibrational analysis. MoS₂ was created in the shape of a flower, and NiO was grown on the layer of the surface to create a heterostructure composite at nanoscale. In the 1 M aqueous solution of KOH, NM10 exhibited a high specific capacitance of 289 F/g and capacitance retention of 101.5% after 2000 GCD cycles. The decreased capacitance may have been caused by the low-cost graphite current collector's resistance. This work makes a compelling case that the combination of EDLC behavior MoS₂ and pseudocapacitance behavior NiO has an effective electrode material for supercapacitors.

Supplementary Materials: The following supporting information can be downloaded at: <https://www.mdpi.com/article/10.3390/en16010335/s1>, Figure S1: EDAX energy spectrum of N, M, NM3, and NM10; Figure S2: GCD specific capacitance for different energy density; Figure S3: TGA of N, M, NM3 and NM10; Figure S4: Photograph of lab scale supercapacitor device; Table S1: Specific capacitance of N, M, NM3, NM10 and NM15 samples at 5 mV/s Scan rate from CV; Table S2: Specific capacitance calculated from GCD techniques; Table S3: Elemental composition of samples.

Author Contributions: D.K.: conceptualization, investigation, data analysis, writing—original draft, writing—review and editing; P.P.: conceptualization discussion; P.M.: writing—editing; B.R.W.: review and editing. A.M.: supervision, validation, writing—review and editing; G.S.: writing—review and editing, validation. All authors have read and agreed to the published version of the manuscript.

Funding: Dhivyaprasath Kasinathan and Preethi Muruganandam are thankful to the Ministry of Education (MoE), India, for financial support through an NIT-Tiruchirappalli GATE institute fellowship. Biny R. Wiston is thankful to the Department of Science and Technology (DST), India, for the financial support through an INSPIRE-SRF fellowship (DST/INSPIRE Fellowship/2014/IF170069).

Data Availability Statement: The data presented in this study are available on request.

Conflicts of Interest: The authors declare no conflict of interest.

References

1. *Global Energy Review 2021*; International Energy Agency (IEA): Paris, France, 2021; p. 36.
2. Dincer, I. Renewable Energy and Sustainable Development: A Crucial Review. *Renew. Sustain. Energy Rev.* **2000**, *4*, 157–175. [[CrossRef](#)]
3. Halper, M.S. *Supercapacitors: A Brief Overview*; The MITRE Corporation: McLean, VA, USA, 2006; p. 41.
4. Vangari, M.; Pryor, T.; Jiang, L. Supercapacitors: Review of Materials and Fabrication Methods. *J. Energy Eng.* **2013**, *139*, 72–79. [[CrossRef](#)]
5. Xiao, J.; Li, H.; Zhang, H.; He, S.; Zhang, Q.; Liu, K.; Jiang, S.; Duan, G.; Zhang, K. Nanocellulose and Its Derived Composite Electrodes toward Supercapacitors: Fabrication, Properties, and Challenges. *J. Bioresour. Bioprod.* **2022**, *7*, 245–269. [[CrossRef](#)]
6. Han, X.; Xiao, G.; Wang, Y.; Chen, X.; Duan, G.; Wu, Y.; Gong, X.; Wang, H. Design and Fabrication of Conductive Polymer Hydrogels and Their Applications in Flexible Supercapacitors. *J. Mater. Chem. A* **2020**, *8*, 23059–23095. [[CrossRef](#)]
7. Wang, Y.; Zhang, L.; Hou, H.; Xu, W.; Duan, G.; He, S.; Liu, K.; Jiang, S. Recent Progress in Carbon-Based Materials for Supercapacitor Electrodes: A Review. *J. Mater. Sci.* **2021**, *56*, 173–200. [[CrossRef](#)]
8. Kuo, S.-L.; Wu, N.-L. Investigation of Pseudocapacitive Charge-Storage Reaction of $\text{MnO}_2 \cdot \text{NH}_2\text{O}$ Supercapacitors in Aqueous Electrolytes. *J. Electrochem. Soc.* **2006**, *153*, A1317. [[CrossRef](#)]
9. Hu, C.-C.; Chang, K.-H.; Lin, M.-C.; Wu, Y.-T. Design and Tailoring of the Nanotubular Arrayed Architecture of Hydrated RuO_2 for Next Generation Supercapacitors. *Nano Lett.* **2006**, *6*, 2690–2695. [[CrossRef](#)]
10. Wu, S.; Hui, K.S.; Hui, K.N.; Kim, K.H. Ultrathin Porous NiO Nanoflake Arrays on Nickel Foam as an Advanced Electrode for High Performance Asymmetric Supercapacitors. *J. Mater. Chem. A* **2016**, *4*, 9113–9123. [[CrossRef](#)]
11. Kumar, R.; Soam, A.; Sahajwalla, V. Carbon Coated Cobalt Oxide ($\text{CC-CO}_3\text{O}_4$) as Electrode Material for Supercapacitor Applications. *Mater. Adv.* **2021**, *2*, 2918–2923. [[CrossRef](#)]
12. Chen, J.; Huang, K.; Liu, S. Hydrothermal Preparation of Octadecahedron Fe_3O_4 Thin Film for Use in an Electrochemical Supercapacitor. *Electrochim. Acta* **2009**, *55*, 1–5. [[CrossRef](#)]
13. Rajendra Prasad, K.; Miura, N. Electrochemical Synthesis and Characterization of Nanostructured Tin Oxide for Electrochemical Redox Supercapacitors. *Electrochem. Commun.* **2004**, *6*, 849–852. [[CrossRef](#)]
14. Wee, G.; Soh, H.Z.; Cheah, Y.L.; Mhaisalkar, S.G.; Srinivasan, M. Synthesis and Electrochemical Properties of Electrospun V_2O_5 Nanofibers as Supercapacitor Electrodes. *J. Mater. Chem.* **2010**, *20*, 6720–6725. [[CrossRef](#)]
15. Vijayakumar, S.; Nagamuthu, S.; Muralidharan, G. Supercapacitor Studies on NiO Nanoflakes Synthesized Through a Microwave Route. *ACS Appl. Mater. Interfaces* **2013**, *5*, 2188–2196. [[CrossRef](#)] [[PubMed](#)]
16. Dhas, S.D.; Maldar, P.S.; Patil, M.D.; Nagare, A.B.; Waikar, M.R.; Sonkawade, R.G.; Moholkar, A.V. Synthesis of NiO Nanoparticles for Supercapacitor Application as an Efficient Electrode Material. *Vacuum* **2020**, *181*, 109646. [[CrossRef](#)]
17. Pore, O.C.; Fulari, A.V.; Parale, V.G.; Park, H.H.; Shejwal, R.V.; Fulari, V.J.; Lohar, G.M. Facile Hydrothermal Synthesis of NiO/RGO Nanocomposite Electrodes for Supercapacitor and Nonenzymatic Glucose Biosensing Application. *J. Porous Mater.* **2022**, *29*, 1991–2001. [[CrossRef](#)]
18. Kong, D.-S.; Wang, J.-M.; Shao, H.-B.; Zhang, J.-Q.; Cao, C. Electrochemical Fabrication of a Porous Nanostructured Nickel Hydroxide Film Electrode with Superior Pseudocapacitive Performance. *J. Alloys Compd.* **2011**, *509*, 5611–5616. [[CrossRef](#)]
19. Li, L.; Yang, H.; Yang, J.; Zhang, L.; Miao, J.; Zhang, Y.; Sun, C.; Huang, W.; Dong, X.; Liu, B. Hierarchical $\text{Carbon}@\text{Ni}_3\text{S}_2@\text{MoS}_2$ Double Core–Shell Nanorods for High-Performance Supercapacitors. *J. Mater. Chem. A* **2016**, *4*, 1319–1325. [[CrossRef](#)]
20. Jeevanandham, G.; Jerome, R.; Murugan, N.; Preethika, M.; VEDIAPPAN, K.; Sundramoorthy, A.K. Nickel Oxide Decorated MoS_2 Nanosheet-Based Non-Enzymatic Sensor for the Selective Detection of Glucose. *RSC Adv.* **2020**, *10*, 643–654. [[CrossRef](#)]
21. Joseph, N.; Shafi, P.M.; Bose, A.C. Recent Advances in 2D- MoS_2 and Its Composite Nanostructures for Supercapacitor Electrode Application. *Energy Fuels* **2020**, *34*, 6558–6597. [[CrossRef](#)]
22. Acerce, M.; Voiry, D.; Chhowalla, M. Metallic 1T Phase MoS_2 Nanosheets as Supercapacitor Electrode Materials. *Nat. Nanotech.* **2015**, *10*, 313–318. [[CrossRef](#)]
23. Joseph, N.; Shafi, P.M.; Bose, A.C. Metallic 1T- MoS_2 with Defect Induced Additional Active Edges for High Performance Supercapacitor Application. *New J. Chem.* **2018**, *42*, 12082–12090. [[CrossRef](#)]
24. Geng, X.; Zhang, Y.; Han, Y.; Li, J.; Yang, L.; Benamara, M.; Chen, L.; Zhu, H. Two-Dimensional Water-Coupled Metallic MoS_2 with Nanochannels for Ultrafast Supercapacitors. *Nano Lett.* **2017**, *17*, 1825–1832. [[CrossRef](#)] [[PubMed](#)]
25. Ghasemi, F.; Jalali, M.; Abdollahi, A.; Mohammadi, S.; Sanaee, Z.; Mohajerzadeh, S. A High Performance Supercapacitor Based on Decoration of MoS_2 /Reduced Graphene Oxide with NiO Nanoparticles. *RSC Adv.* **2017**, *7*, 52772–52781. [[CrossRef](#)]
26. Li, Z.; Qin, Z.; Zhang, W.; Li, Z. Controlled Synthesis of $\text{Ni}(\text{OH})_2/\text{MoS}_2$ Nanohybrids for High-Performance Supercapacitors. *Mater. Chem. Phys.* **2018**, *209*, 291–297. [[CrossRef](#)]
27. Luo, W.; Zhang, G.; Cui, Y.; Sun, Y.; Qin, Q.; Zhang, J.; Zheng, W. One-Step Extended Strategy for the Ionic Liquid-Assisted Synthesis of $\text{Ni}_3\text{S}_4\text{-MoS}_2$ Heterojunction Electrodes for Supercapacitors. *J. Mater. Chem. A* **2017**, *5*, 11278–11285. [[CrossRef](#)]

28. Yue, L.; Wang, X.; Sun, T.; Liu, H.; Li, Q.; Wu, N.; Guo, H.; Yang, W. Ni-MOF Coating MoS₂ Structures by Hydrothermal Intercalation as High-Performance Electrodes for Asymmetric Supercapacitors. *Chem. Eng. J.* **2019**, *375*, 121959. [[CrossRef](#)]
29. Kumar, C.; Das, S.; Jit, S. 7—Device Physics and Device Integration of Two-Dimensional Heterostructures. In *2D Nanoscale Heterostructured Materials*; Jit, S., Das, S., Eds.; Micro and Nano Technologies; Elsevier: Amsterdam, The Netherlands, 2020; pp. 195–214, ISBN 978-0-12-817678-8.
30. Saha, S.; Samanta, P.; Murmu, N.C.; Kuila, T. A Review on the Heterostructure Nanomaterials for Supercapacitor Application. *J. Energy Storage* **2018**, *17*, 181–202. [[CrossRef](#)]
31. Wang, K.; Yang, J.; Zhu, J.; Li, L.; Liu, Y.; Zhang, C.; Liu, T. General Solution-Processed Formation of Porous Transition-Metal Oxides on Exfoliated Molybdenum Disulfides for High-Performance Asymmetric Supercapacitors. *J. Mater. Chem. A* **2017**, *5*, 11236–11245. [[CrossRef](#)]
32. Ci, S.; Wen, Z.; Qian, Y.; Mao, S.; Cui, S.; Chen, J. NiO-Microflower Formed by Nanowire-Weaving Nanosheets with Interconnected Ni-Network Decoration as Supercapacitor Electrode. *Sci. Rep.* **2015**, *5*, 11919. [[CrossRef](#)]
33. Rasamani, K.D.; Alimohammadi, F.; Sun, Y. Interlayer-Expanded MoS₂. *Mater. Today* **2017**, *20*, 83–91. [[CrossRef](#)]
34. Sahu, T.S.; Mitra, S. Exfoliated MoS₂ Sheets and Reduced Graphene Oxide—An Excellent and Fast Anode for Sodium-Ion Battery. *Sci. Rep.* **2015**, *5*, 12571. [[CrossRef](#)] [[PubMed](#)]
35. Yang, L.; Cui, X.; Zhang, J.; Wang, K.; Shen, M.; Zeng, S.; Dayeh, S.A.; Feng, L.; Xiang, B. Lattice Strain Effects on the Optical Properties of MoS₂ Nanosheets. *Sci. Rep.* **2014**, *4*, 5649. [[CrossRef](#)] [[PubMed](#)]
36. Swain, G.; Sultana, S.; Naik, B.; Parida, K. Coupling of Crumpled-Type Novel MoS₂ with CeO₂ Nanoparticles: A Noble-Metal-Free p–n Heterojunction Composite for Visible Light Photocatalytic H₂ Production. *ACS Omega* **2017**, *2*, 3745–3753. [[CrossRef](#)] [[PubMed](#)]
37. Zheng, J.; Zhang, R.; Wang, X.; Yu, P. Importance of Carbon Quantum Dots for Improving the Electrochemical Performance of MoS₂@ZnS Composite. *J. Mater. Sci.* **2019**, *54*, 13509–13522. [[CrossRef](#)]
38. Patterson, A.L. The Scherrer Formula for X-ray Particle Size Determination. *Phys. Rev.* **1939**, *56*, 978–982. [[CrossRef](#)]
39. Siddique, M.N.; Ahmed, A.; Ali, T.; Tripathi, P. Investigation of Optical Properties of Nickel Oxide Nanostructures Using Photoluminescence and Diffuse Reflectance Spectroscopy. *AIP Conf. Proc.* **2018**, *1953*, 030027. [[CrossRef](#)]
40. Mihaylov, M.; Chakarova, K.; Hadjiivanov, K. Formation of Carbonyl and Nitrosyl Complexes on Titania- and Zirconia-Supported Nickel: FTIR Spectroscopy Study. *J. Catal.* **2004**, *228*, 273–281. [[CrossRef](#)]
41. Ritika, Kaur, M.; Umar, A.; Mehta, S.K.; Singh, S.; Kansal, S.K.; Fouad, H.; Alothman, O.Y. Rapid Solar-Light Driven Superior Photocatalytic Degradation of Methylene Blue Using MoS₂-ZnO Heterostructure Nanorods Photocatalyst. *Materials* **2018**, *11*, 2254. [[CrossRef](#)]
42. Vishnoi, P.; Sampath, A.; Waghmare, U.V.; Rao, C.N.R. Covalent Functionalization of Nanosheets of MoS₂ and MoSe₂ by Substituted Benzenes and Other Organic Molecules. *Chem. Eur. J.* **2017**, *23*, 886–895. [[CrossRef](#)]
43. Wiston, B.R.; Ashok, M. Microwave-Assisted Synthesis of Cobalt-Manganese Oxide for Supercapacitor Electrodes. *Mater. Sci. Semicond. Process.* **2019**, *103*, 104607. [[CrossRef](#)]
44. Mathis, T.S.; Kurra, N.; Wang, X.; Pinto, D.; Simon, P.; Gogotsi, Y. Energy Storage Data Reporting in Perspective—Guidelines for Interpreting the Performance of Electrochemical Energy Storage Systems. *Adv. Energy Mater.* **2019**, *9*, 1902007. [[CrossRef](#)]
45. Kumuthini, R.; Ramachandran, R.; Therese, H.A.; Wang, F. Electrochemical Properties of Electrospun MoS₂@C Nanofiber as Electrode Material for High-Performance Supercapacitor Application. *J. Alloys Compd.* **2017**, *705*, 624–630. [[CrossRef](#)]
46. Wang, B.; Chen, J.S.; Wang, Z.; Madhavi, S.; Lou, X.W. Green Synthesis of NiO Nanobelts with Exceptional Pseudo-Capacitive Properties. *Adv. Energy Mater.* **2012**, *2*, 1188–1192. [[CrossRef](#)]
47. Zhang, Z.J.; Xie, D.H.; Cui, P.; Chen, X.Y. Conversion of a Zinc Salicylate Complex into Porous Carbons through a Template Carbonization Process as a Superior Electrode Material for Supercapacitors. *RSC Adv.* **2014**, *4*, 6664. [[CrossRef](#)]
48. Prakash, D.; Manivannan, S. N, B Co-Doped and Crumpled Graphene Oxide Pseudocapacitive Electrode for High Energy Supercapacitor. *Surf. Interfaces* **2021**, *23*, 101025. [[CrossRef](#)]
49. Li, S.; Chen, T.; Wen, J.; Gui, P.; Fang, G. In Situ Grown Ni₉S₈ Nanorod/O-MoS₂ Nanosheet Nanocomposite on Carbon Cloth as a Free Binder Supercapacitor Electrode and Hydrogen Evolution Catalyst. *Nanotechnology* **2017**, *28*, 445407. [[CrossRef](#)] [[PubMed](#)]
50. Qin, Q.; Chen, L.; Wei, T.; Liu, X. MoS₂/NiS Yolk-Shell Microsphere-Based Electrodes for Overall Water Splitting and Asymmetric Supercapacitor. *Small* **2019**, *15*, 1803639. [[CrossRef](#)]
51. Zheng, S.; Zhang, J.; Deng, H.; Du, Y.; Shi, X. Chitin Derived Nitrogen-Doped Porous Carbons with Ultrahigh Specific Surface Area and Tailored Hierarchical Porosity for High Performance Supercapacitors. *J. Bioresour. Bioprod.* **2021**, *6*, 142–151. [[CrossRef](#)]
52. Guo, W.; Guo, X.; Yang, L.; Wang, T.; Zhang, M.; Duan, G.; Liu, X.; Li, Y. Synthetic Melanin Facilitates MnO Supercapacitors with High Specific Capacitance and Wide Operation Potential Window. *Polymer* **2021**, *235*, 124276. [[CrossRef](#)]
53. Wei, L.; Deng, W.; Li, S.; Wu, Z.; Cai, J.; Luo, J. Sandwich-like Chitosan Porous Carbon Spheres/MXene Composite with High Specific Capacitance and Rate Performance for Supercapacitors. *J. Bioresour. Bioprod.* **2022**, *7*, 63–72. [[CrossRef](#)]
54. Li, H.; Liu, Y.-L.; Jin, H.; Cao, L.; Yang, H.; Jiang, S.; He, S.; Li, S.; Liu, K.; Duan, G. Bimetallic Salts Template-Assisted Strategy towards the Preparation of Hierarchical Porous Polyimide-Derived Carbon Electrode for Supercapacitor. *Diam. Relat. Mater.* **2022**, *128*, 109283. [[CrossRef](#)]

55. Cao, L.; Li, H.; Xu, Z.; Gao, R.; Wang, S.; Zhang, G.; Jiang, S.; Xu, W.; Hou, H. Camellia Pollen-Derived Carbon with Controllable N Content for High-Performance Supercapacitors by Ammonium Chloride Activation and Dual N-Doping. *ChemNanoMat* **2021**, *7*, 34–43. [[CrossRef](#)]
56. Wang, F.; Chen, L.; Li, H.; Duan, G.; He, S.; Zhang, L.; Zhang, G.; Zhou, Z.; Jiang, S. N-Doped Honeycomb-like Porous Carbon towards High-Performance Supercapacitor. *Chin. Chem. Lett.* **2020**, *31*, 1986–1990. [[CrossRef](#)]

Disclaimer/Publisher’s Note: The statements, opinions and data contained in all publications are solely those of the individual author(s) and contributor(s) and not of MDPI and/or the editor(s). MDPI and/or the editor(s) disclaim responsibility for any injury to people or property resulting from any ideas, methods, instructions or products referred to in the content.